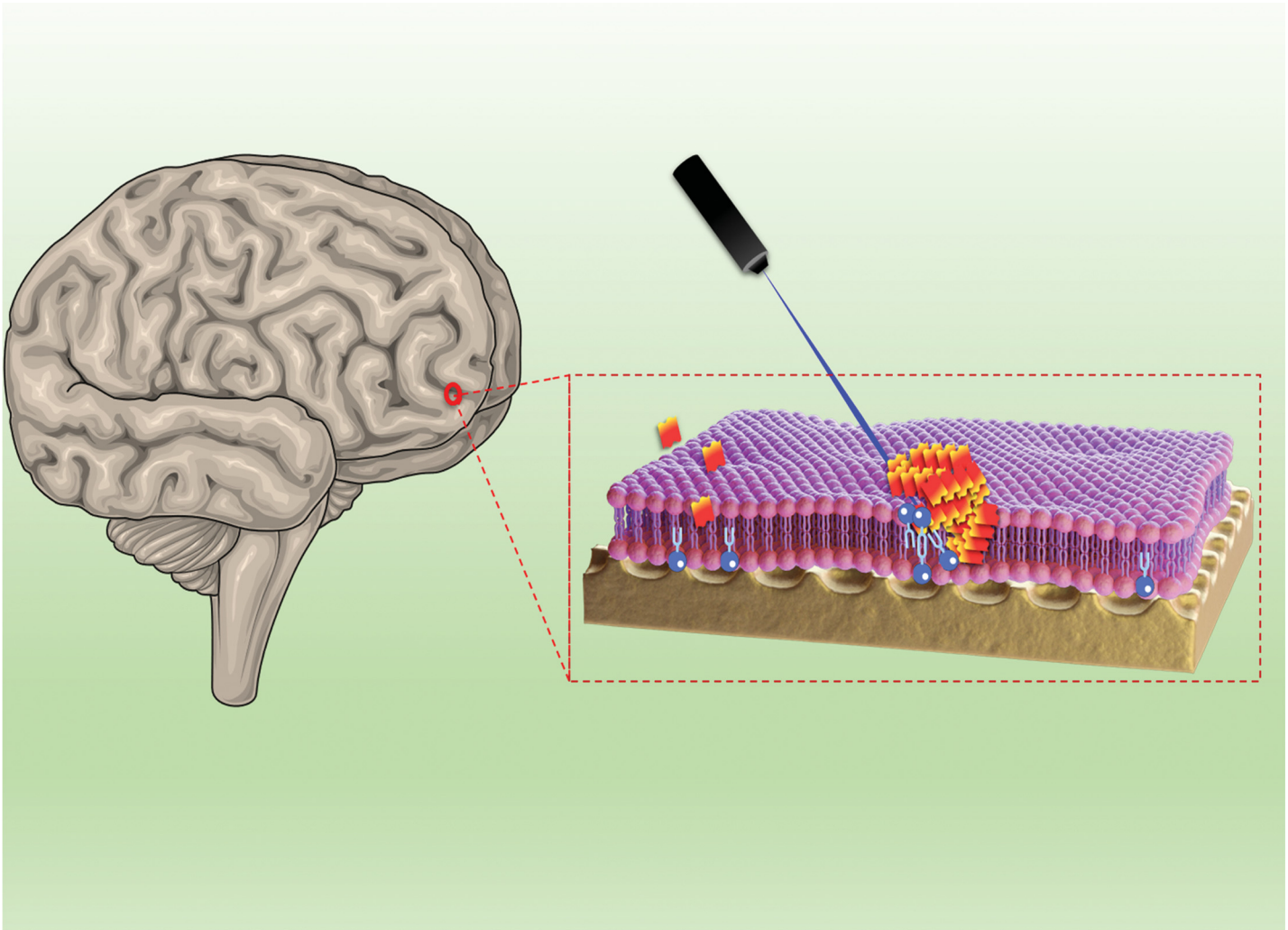

Showcasing the research from the group of Professor Tia E Keyes, Dublin City University, Ireland

Role of phosphatidylserine in amyloid-beta oligomerization at asymmetric phospholipid bilayers

The Keyes lab has been working on imprinted microporous suspended lipid bilayers (MSLB), which are a real biomimetic membrane model due to their dual-aspect fluidity, addressability, and compositional diversity. Current work elucidates how laser damage triggers amyloid-beta binding and oligomer formation by translocating phosphatidylserine, an abundant lipid in neuronal membranes, from the inner leaflet to the outer leaflet of a symmetric MSLB using EIS.

The brain icon in the cover art is adopted and modified from bioicons Servier https://smart.servier.com

As featured in:

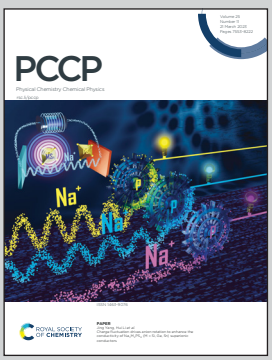

See Tia E. Keyes *et al.*, *Phys. Chem. Chem. Phys.*, 2023, **25**, 7648.

ROYAL SOCIETY OF CHEMISTRY

rsc.li/pccp

Registered charity number: 207890

PCCP

ROYAL SOCIETY OF CHEMISTRY

PAPER

View Article Online
View Journal | View Issue

Cite this: *Phys. Chem. Chem. Phys.*, 2023, **25**, 7648

Role of phosphatidylserine in amyloid-beta oligomerization at asymmetric phospholipid bilayers†

Jack Robinson, ‡[a] Nirod Kumar Sarangi ‡[ab] and Tia E. Keyes *[ab]

Amyloid-beta ($A\beta_{1-42}$) aggregation triggers neurotoxicity and is linked to Alzheimer's disease. $A\beta_{1-42}$ oligomers, rather than extended fibrils, adhere to the cell membrane, causing cell death. Phosphatidylserine (PS), an anionic phospholipid, is prevalent in neuronal membranes (< 20 molar percentage) and, while isolated to the cytoplasmic leaflet of the membrane in healthy cells, its exposure in apoptotic cells and migration to exoplasmic leaflet is triggered by oxidative damage to the membrane. It is widely believed that PS plays a crucial role in the Aβ peptide interaction in the membranes of neuronal cells. However, due to the complexity of the cell membrane, it can be challenging to address molecular level understanding of the PS-Aβ binding and oligomerization processes. Herein, we use microcavity supported lipid bilayers (MSLBs) to analyse PS and $A\beta_{1-42}$ binding, oligomer formation, and membrane damage. MSLBs are a useful model to evaluate protein–membrane interactions because of their cell-like dual aspect fluidity, their addressability and compositional versatility. We used electrochemical impedance spectroscopy (EIS) and confocal fluorescence microscopy to compare the impact of $A\beta_{1-42}$ on simple zwitterioinic membrane, dioleoylphosphatidylcholine (DOPC), with MSLBs comprised of transversally asymmetric binary DOPC and dioleoylphosphatidylserine (DOPS). Monomeric $A\beta_{1-42}$ adsorbs weakly to the pristine zwitterionic DOPC membrane without aggregation. Using a membrane integrity test, with pyranine trapped within the cavities beneath the membrane, $A\beta_{1-42}$ exposure did not result in pyranine leakage, indicating that DOPC membranes were intact. When 10 mol% DOPS was doped asymmetrically into the membrane's outer leaflet, oligomerization of $A\beta_{1-42}$ monomer was evident in EIS and atomic force microscopy (AFM), and confocal imaging revealed that membrane damage, resulted in extensive pyranine leakage from the pores. The effects were time, and DOPS and $A\beta_{1-42}$ concentration-dependent. Membrane pore formation was visible within 30 minutes, and oligomerization, membrane-oligomer multilayer, and $A\beta_{1-42}$ fibril formation evident over 3 to 18 hours. In asymmetric membranes with DOPS localized to the lower leaflet, optothermally (laser induced) damage increased local DOPS concentrations at the distal leaflet, promoting $A\beta_{1-42}$ aggregation.

Received 21st July 2022,
Accepted 21st October 2022

DOI: 10.1039/d2cp03344e

rsc.li/pccp

Introduction

Alzheimer's disease (AD) is the most common form of dementia. Mainly associated with older adults, it is an irreversible brain disorder that causes progressive and irreversible loss of cognitive function.[1] Amyloid-fibrils in AD are generated from amyloid-beta (Aβ), a naturally secreted peptide, found in various isoforms of different lengths. Among the isoforms, the 40 residue ($A\beta_{1-40}$) constitutes the most common Aβ isoform in the brain, and the 42 residue ($A\beta_{1-42}$) exhibits a considerable rise in some kinds of AD.[2] Aβ has been detected in its oligomeric form in the cerebrospinal fluid and brain homogenates of Alzheimer's patients in the femto to picomolar range.[3,4] There is substantial evidence indicating that the self-aggregation of monomeric Aβ to fibrils, particularly oligomers, plays an important role in the progression of AD.[5–8] Although there is still debate over the amyloid model and the relative roles of tau and amyloid in disease progression, the recent FDA approval of Aducanumab suggests causality, although the drug is not currently approved by the European Medicines Agency.[9] In AD, Aβ peptide is released from cells by the action of β- and γ-secretases on amyloid precursor protein (APP), where it undergoes amyloidogenesis; aggregation to oligomers, multimers, and

[a] *School of Chemical Sciences, Dublin City University, Dublin 9, Ireland*
[b] *National Center for Sensor Research, Dublin City University, Dublin 9, Ireland. E-mail: tia.keyes@dcu.ie*

† Electronic supplementary information (ESI) available: Detailed fabrication methods, bilayer stability studies, confocal fluorescence and additional AFM data are provided. See DOI: https://doi.org/10.1039/d2cp03344e

‡ These authors contributed equally to this work.

fibrils in the extracellular space, eventually forming the plaques that are characteristic of the disease.[10] Furthermore, pathogenic amyloid aggregates are not confined to AD but also play a major role in Parkinson's, Huntington's, and Diabetes.[11] Aβ peptides are composed of 36 to 43 amino acids that spontaneously self-aggregate through hydrophobic-hydrophobic interactions, especially at higher concentrations (micro to submillimolar range).[12–14] All amyloid aggregates can serve as cellular hallmarks for AD; however, soluble, small oligomers formed from $A\beta_{1-42}$ have recently been shown to be more toxic than larger fibrils.[15,16] Because AD currently has no cure and cannot be prevented, models that can improve understanding of the mechanisms behind Aβ aggregation can provide insights into early detection strategies, understanding of possible preventative strategies and the development of therapy.[16,17] Furthermore, given the prevalence of amyloid aggregation in numerous disease conditions beyond AD, tools to investigate Aβ aggregation are broadly important. The current understanding of amyloid action at the cellular interface is based on in-cellulo that have either targeted specific receptors or examined non-specific interactions with lipids within membranes in biophysical models.[18,19] Numerous *in vitro* studies have revealed that the lipidic membrane in general, and negatively charged phospholipids like phosphatidylserine (PS) in particular, can promote Aβ oligomer formation at the bilayer interface.[16,20–24] Aβ oligomers can develop in solution at high concentrations (μM to mM) due to self-assembly, while at low concentrations (pM to nM), oligomers form upon interaction with the lipidic interface. Of note, Aβ oligomers have the ability to disrupt cell membrane integrity and permeability.[21,22,24–26]

To date, a number of models have been proposed to explain Aβ oligomer induced membrane toxicity, for example, (a) the poration model, proposes that amyloid forms stable transmembrane pores at the neuronal membrane, disrupting intracellular Ca^{2+} homeostasis; (b) the carpet model, hypothesizes that amyloid adsorption at the membrane interface destabilizes the membrane structure; and (c) the membrane dissolution model, hypothesizes amyloid precipitates serve as detergent, stripping off lipid from the bilayer.[17,27,28] In all of these models, membrane disruption can result in oxidative stress, a key effector in AD progression that leads to cellular apoptosis.[29–32] Under conditions of oxidative stress, phosphatidylserine, which is normally confined to the cytosolic leaflet of the lipid bilayer in the naturally asymmetric neuronal membrane, migrates to the extracellular leaflet. This is a primary step in the onset of apoptosis, and a number of studies have indicated that anionic lipids, particularly PS, influence Aβ oligomerization, fibrilization, and fibril growth.[33–39] PS is particularly important as it is prevalent at the plasma membrane of neuronal cells, where Aβ peptide interaction occurs.[40] The electrostatic attraction between positively charged Aβ and negatively charged PS is the primary driving force.[41–43] And, while there is significant evidence, notably from *in vitro* models, that Aβ and PS interaction has a role in inducing the formation of oligomer scaffold,[44–48] other membrane factors such as cholesterol content, membrane packing density, and lipid rafts also play a role.[15,21,49–53] Kim *et al.* recently reported on the impact of different anionic phospholipids, such as dioleoyl phosphatidylserine (DOPS) or dioleoyl phosphatidylglycerol (DOPG), and mixed vesicles of DOPC/DOPS and DOPC/DOPG on the formation of Aβ fibrils. They observed that the liposome packing density (regulated by varying fatty acid on the PS in terms of length and unsaturation) and the DOPS/DOPG ratio, influenced the rate of fibrinogenesis and the length of the resulting fibrils.[54] Although the concentration of PS in natural membranes was much greater than anticipated, the study showed the impact of membrane packing/fluidity and charge on amyloidgenisis.

Such biophysical models of the lipid membrane have provided deep insights into Aβ-cell membrane interactions because they permit a reductionist approach, separating the variables that affect oligomer growth at membranes. Aβ-membrane interactions have been studied using a diverse of models, including liposomes, black lipid membranes, and supported lipid bilayer membranes (SLBs).[3,22,37,55–59] However, there are challenges in addressing some aspects of Aβ interaction. Liposomes for example, have a lack of control over compositional asymmetry, and are generally not addressable with surface-sensitive analytical tools. Substrate supported lipid bilayers (SLBs) and their variants address these issues, but they suffer different limitations, particularly in the study of dynamics of membrane/protein interactions that require lateral or transversal diffusion of lipid or components due to frictional lipid-substrate or protein/peptide-substrate interaction, which hinders diffusion and can even lead to protein/peptide denaturation.[60–64] Although all of these models have provided crucial insights on Aβ-membrane interaction, the impact of varying PS concentrations within the physiological concentration limit and its asymmetric distribution across the bilayer on the recognition and assembly of Aβ, as well as the associated kinetics of oligomer formation under these conditions, has not yet been fully explored.

In this context, microcavity supported lipid bilayers (MSLBs) in combination with electrochemical impedance spectroscopy (EIS) offer a useful approach. The microcavity pore provides aqueous reservoirs at each lipid leaflet interface, avoiding any loss of activity or assembly of peptide due to friction, and the layer by layer approach to fabrication enables facile and precise building of asymmetry into the bilayers structure with transversal fluidity that is expected to be cell-like.[33,34] EIS is a sensitive, label-free technique that, by measuring changes to the admittance of bilayer membrane, can reveal details of molecular mechanism of Aβ activity in real time.

Exploiting these methods, herein, we study the role of DOPS content within DOPC on membrane association and assembly of $A\beta_{1-42}$. At a fixed concentration of $A\beta_{1-42}$ (1 μM) and using EIS, we established that 10 mol% DOPS is sufficient to facilitate Aβ oligomerization without damaging the membrane. At 5 mol% DOPS, no large-scale perturbation of membrane or oligomer formation is detected in the presence of $A\beta_{1-42}$ (1 μM). However, at membranes comprising 20 mol% of DOPS, the activity of $A\beta_{1-42}$ triggered the assembly processes leading to membrane damage. Atomic force microscopy (AFM) and confocal microscopy imaging were used to further identify large-scale oligomer formation and membrane damaging effect caused by $A\beta_{1-42}$. As PS is localized to the cytoplasmic leaflet of the neuronal

membrane in homeostatic cells and only migrates during membranal damage, *e.g.*, under oxidative stress, we induced optothermal damage to mimic this process and observed that DOPS transverse diffusion stimulated $A\beta_{1-42}$ assembly.

Experimental

Materials

1,2-Dioleoyl-*sn*-glycero-3-phosphocholine (DOPC) and 1,2-dioleoyl-*sn*-glycero-3-phospho-L-serine (DOPS) were purchased with maximum degree of purity (<99%) from Avanti Polar Lipids (Alabama, USA) and used without further purification. 1,2-Dioleoyl-*sn*-glycero-3-phosphoethamine labelled Atto655 (DOPE-Atto655) was purchased from ATTO-TEC GmbH (Siegen, Germany). HEPES salt and sodium azide were purchased from Sigma-Aldrich (Wicklow, Ireland). Amyloid beta ($A\beta_{1-42}$) was purchased from Biolegend UK Ltd (London,UK). Gold on silicon wafers were purchased from Ams Biotechnology (Abingdon, UK). Polybead microspheres of different sizes were purchased from Polysciences Europe Gmbh (Baden-Württemberg, Germany). Aqueous solutions were prepared using MilliQ water (18 mΩ cm) (Milipore Corp. Bedford, USA). Polydimethylsiloxane silicon elastomer (PDMS) was purchased from Dow Corning Gmbh (Wiesbaden, Germany) and mixed following supplier's instructions. 1,1,1,3,3,3-Hexafluoroisopropanol (HFIP) and Thioflavin T (Tht) were purchased from Sigma-Aldrich (Wicklow, Ireland). Beta Amyloid (1–42) HiLyte^{TM} Fluoro 555 (Aβ555) was purchased from Eurogentec (Seraing, Belgium).

Methods

Instrumentation. Hitachi 3400 Scanning Electron Microscope was used to image the MSLB array during fabrication. Lipid monolayer formation by Langmuir–Blodgett was performed using NIMA 102D Langmuir–Blodgett trough. Electrochemical Impedance Spectroscopy was performed using a CH Instrument model 760E Electrochemical Workstation, with a three-electrode cell, Ag/AgCl (1M KCl) reference electrode, platinum wire auxiliary electrode and the MSLB as the working electrode. Equivalent circuit models were fit to raw data using Scribner Z-View software. A 405 nm diode laser, 3.12 mW, was applied for 10 s, to photodamage the bilayer.[61] All absorbance measurements were performed with a Jasco V670 Spectrophotometer (Jasco Spectra Manager v2 software). Emission spectra were obtained using a Varian Cary Eclipse Fluorescence Spectrophotometer (Varian Cary Eclipse Software v1.1). The excitation and emission slit widths were set to 10 nm unless stated otherwise. Confocal imaging was carried out on a Leica TSP DMi8 confocal microscope with 63× oil immersion objective lens unless stated otherwise.

Gold microcavity array fabrication and bilayer assembly. Gold microcavity (1 μm) arrays were prepared following the method previously reported by Keyes *et al.* and detailed in ESI† (Fig. S1).[61–68] The following lipid bilayer compositions were used in this work: symmetric DOPC lipid bilayer with DOPC in both leaflets, asymmetric DOPC : DOPS (80 : 20)//DOPC, DOPC : DOPS (90 : 10)//DOPC or DOPC : DOPS (95 : 5)//DOPC, lipid bilayers where the distal leaflet is composed of 80 mol% DOPC and 20 mol% of DOPS (or 90 mol% DOPC and 10 mol% DOPS, or 95 mol% DOPC and 5 mol% DOPS) while the proximal leaflet is composed of 100 mol% of DOPC to model an apoptotic cell membrane. The double forward slash ''//'' indicates the two monolayers of different composition in the bilayer, the distal (away from substrate, at the bulk aqueous interface) leaflet and proximal leaflet (closest to substrate) of the designated membrane. Similarly, the other sets of asymmetric membranes such as DOPC//DOPC : DOPS (80 : 20), DOPC//DOPC : DOPS (90 : 10) or DOPC//DOPC : DOPS (95 : 5) contain 100 mol% DOPC at distal leaflet and proximal leaflet with varied DOPC : DOPS compositions including 80 mol% DOPC and 20 mol% of DOPS, 90 mol% DOPC and 10 mol% of DOPS, and 95 mol% DOPC and 5 mol% DOPS, as an analogue of a non-apoptotic cell membrane. Microcavity supported lipid bilayers (MSLBs) were assembled across aqueous buffer filled gold microcavity array using a combination of the Langmuir–Blodgett and vesicle fusion (LB-VF) methods. Successful formation of the MSLB across the gold microcavity array was confirmed using fluorescence life-time imaging microscopy (Fig. S1B–D, ESI†) by selectively labelling each layer with a different fluorophore so that each individual leaflet could be imaged separately and confirmed to form a continuous bilayer film across the array.

Amyloid-beta 1–42 ($A\beta_{1-42}$) pre-treatment. For controlled aggregation investigations it is essential to destroy any plausible preformed aggregates.[37,69–72] This was accomplished by dissolving, 1 mg of $A\beta_{1-42}$ in 1 mL of HFIP. After that the 1 mg mL^{-1} peptide solution was aliquoted out into smaller concentration fractions and the HFIP was allowed to evaporate completely under vacuum, because HFIP is a volatile and corrosive alcohol and incompatible with *in vitro* or cell-based studies. The peptides form a thin coating on the sidewall of the Eppendorf tube after HFIP evaporation and are stored at −20 °C for later use. Just before experimentation, the thin film was resuspended in HEPES buffer.[50,57,72–74] Fluorescently labeled peptide (Aβ555) was subjected to a similar pre-treatment in order to eliminate any preformed aggregates.

Electrochemical impedance spectroscopy. Electrochemical impedance spectroscopy (EIS) was performed using a CH Instrument model 760E Electrochemical Workstation as potentiostat and a three electrode cell with a platinum wire auxiliary electrode, an Ag/AgCl reference electrode, and gold microcavity array as the working electrode. EIS was measured over a frequency range of 10 000 Hz to 0.01 Hz with an AC modulation amplitude of 0.01 V at a potential bias of 0 V (*vs.* Ag/AgCl). All measurements were performed in a glass cell (approximate volume of 5 mL) in HEPES buffer at pH 7.4. The MSLB with the desired bilayer was initially analyzed prior to the addition of $A\beta_{1-42}$ to ensure signal stability. Resuspended $A\beta_{1-42}$ was then added into the glass cell with HEPES buffer at pH 7.4. The EIS response of the bilayer in contact with $A\beta_{1-42}$ was measured every 30 minutes for 20 hours. Each measurement takes 10 minutes and was carried out at room temperature (20 ± 1 °C). An equivalent circuit model (ECM) was used to fit the measured AC impedance data using Z-View software to estimate

the membrane resistivity and capacitance, as reported previously.[61,66,75] The ECM model is shown in Fig. S2 (ESI†), where R_S, R_M, R_C are resistance of the solution, membrane and cavity array respectively, CPEc + dl is the electrode double layer constant phase element and CPE_M is the constant phase element of the membrane. Constant phase elements ($CPE = 1/Q(j\omega)^m$) were used instead of pure capacitors to account for defects/inhomogeneities in the cavity array electrode and the bilayers. The ECM provided an excellent fit of the measured EIS data across the whole frequency range. When the impedance response was fitted, the only elements that changed significantly on incubation with $A\beta_{1-42}$ were R_M and CPE_M, indicating that the model is valid. During the fit, the CPE exponent, m for membrane and cavity array was found to be 0.94 ± 0.02 and 0.5 ± 0.01 respectively.

Atomic force microscopy. Atomic force microscopy (AFM) imaging of lipid bilayers were carried out using the Veeco Bioscope II system (Nanotec House, Cambridge) coupled with a Zeiss Axiovert inverted optical microscope IX70. Topographic AFM images were obtained in HEPES buffer in tapping mode, using silicon nitride cantilevers PNP-TR-20 (NANO WORLD) with a nominal force constant of 0.32 N m^{-1} and a tip radius of 20 nm. During image acquisition, the resonance frequency in buffer was kept as low as possible, and the scan rate was kept at 0.5 Hz. For AFM studies lipid bilayers were prepared on freshly cleaved mica using the same protocol as used for the MSLB substrates; a DOPC monolayer was deposited by the Langmuir–Blodgett (LB) method followed by vesicle fusion (VF) of liposomes of the following compositions; DOPC, DOPC : DOPS (90 : 10) and DOPC : DOPS (95 : 5). The detailed procedure is provided in ESI.† All AFM images were analyzed using Nanoscope 7.30 software, and the whole images were plane fitted with a 1st order polynomial.

Confocal fluorescence imaging. Confocal fluorescence studies were carried out on MSLBs formed at optically transparent PDMS arrays according to previously reported procedures.[61–63,76,77] In Brief, 50 μL of 4.6 μm polystyrene microspheres (0.1 wt% v/v in ethanol) were drop cast onto squared mica sheet (1 cm^2), which was then attached to a glass coverslip. The spheres were allowed to dry for 1 hour. After that PDMS was poured over the spheres containing mica and thermally cured at 90 °C for 30 minutes to an hour. The polystyrene microspheres (4.6 μm) were removed from the cured PDMS by sonicating the substrates in THF for 30 minutes. The arrays were left to dry overnight to ensure that all of the THF had evaporated. The resulting hexagonally packed PDMS pore array had a pore aperture diameter of 2 μm, which was double that of gold based microcavity array, to faciliate microscopy. Prior to lipid bilayer deposition, the array was air plasma cleaned and sonicated for 30 minutes in 4-(2-Hydroxyethyl)piperazine-1-ethanesulfonic acid (HEPES) buffer (10 mM HEPES salt, 150 mM NaCl, 2 mM NaN_3) at pH 7.4, to ensure buffer filling of micro-pores.[78] MSLBs were then assembled across the PDMS microcavity array using the LB-VF method as described previously and above. The solution of large unilamellar vesicles (LUVs) used for the outer membrane leaflet, contained a mixture of unlabelled lipids and fluorescently labelled phospholipid, DOPE-Atto655 (Ex: 640 nm, detection window 650–780 nm) in a molar ratio of 50 000 : 1, prepared as previously reported.[61,63] Confocal imaging was carried out using a Leica TSP DMi8 confocal microscope in sequential mode with ''between frames'', where the first laser scans the entire spatial x-y region, followed by the second laser scanning the same region, and so on until all the lasers have scanned, and a 63× oil immersion objective lens was used to image the resulting arrays. By pre-sonicating the microcavity array in a 5 μM pyranine solution of HEPES, membrane impermeable probe pyranine was introduced into the pores of the array ahead of bilayer assembly. The pyranine was excited at 405 nm and emission detected between 440 and 560 nm.[62] Aβ555 at the designated concentration was allowed to interact with the PDMS spanning membrane and was excited at 561 nm with a detection window of 570–630 nm. 20 μM Thioflavin T (tht) was dissolved in the contact solution from EIS studies (HEPES buffer used for the electrochemical cell) and excited at 405 nm with a detection window 430–580 nm.

Results and discussion

Effect of $A\beta_{1-42}$ on a symmetric zwitterionic DOPC membrane

In a recent report, on supercritical angle fluorescence measurements of Aβ oligomerization at a DOPC/DOPS (65/35) membrane, Seeger *et al.*[55] hypothesized the following steps: (1) Aβ monomer adsorbs at the membrane, facilitated by long-range electrostatic interactions with anionic lipids; (2) Aβ monomers diffuse along the membrane and self-aggregate, concomitantly inducing lipid clustering that generate nanopores within the membrane, causing additional membrane strain; (3) further aggregation of Aβ removes some of the lipids that are tightly bound to the oligomer scaffold; and (4) the oligomer of Aβ is ejected from the membrane as a plaque leaving a porated/damaged membrane as shown schematically in Fig. 1.[17,26–28,55]

A central tenet of this and other hypotheses is that the membrane becomes porous on amyloid aggregation. Electrochemical impedance spectroscopy (EIS) is a highly sensitive method for exploring such effects because it directly addresses the admittance of the bilayer and was thus used here to distinguish membrane resistance and capacitance changes induced by the Aβ peptide following adsorption, and oligomerization. First to establish the electrochemical characteristics of the membrane prior to exposure to $A\beta_{1-42}$, non-Faradaic EIS measurements were carried out on symmetric DOPC bilayers. The DOPC membrane was prepared by LB-VF method and spanned across the gold microcavity array, which serves as the working electrode in a three electrode cell. Representative non-Faradaic Nyquist plots of DOPC MSLB in the absence and presence of 1 μM $A\beta_{1-42}$ in the contact buffer at different time intervals are shown in Fig. S3 (ESI†). The corresponding data was modeled using an ECM, reported previously (*cf.* Fig. S2, ESI†) to extract the membrane resistance and capacitance values. The absolute values of membrane resistance and capacitance across multiple replicates are respectively 40–60 MΩ cm^2 and 0.6–0.9 μF cm^{-2}. As the microcavity pore arrays are fabrication across a

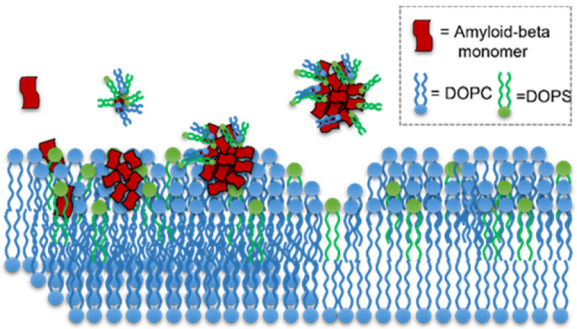

Fig. 1 Hypothesized mechanism of amyloid-beta activity within a lipid bilayer proposed by Seeger *et al.*[55] The majority of the membrane is made up of zwitterionic lipids (blue), and the amyloid beta peptide monomer (red) may adsorb to the membrane. Negatively charged lipids (green) attract amyloid beta peptides, causing the monomers to assemble within the membrane; however, some monomers may pull lipids from the membrane. Within the membrane, the monomers continue to aggregate and form oligomers. Amyloid-beta fibrils fall out of the membrane as a plaque, causing damage to the membrane.

$\sim$1 cm $\times$ 1.5 cm flat gold substrate, and show some batch to batch variation in electrode area due to cavity packing and thiol modification, instead of normalizing with respect to the electroactive area, the mean (N = 3) of relative resistance/capacitance changes with and without the presence of Aβ_{1-42} are reported in Fig. 2. The relative membrane resistance (ΔR_M) is defined as $R_M^{time=t} - R_M^{time=0}$; where $R_M^{time=t}$ is the resistance at time, t and $R_M^{time=0}$ is the resistance at time, 0 *i.e.*, after bilayer preparation. Similarly, ΔCPE_M are defined as, $CPE_M^{time=t} - CPE_M^{time=0}$.

To evaluate membrane stability, impedance spectra were collected every 30 minutes for 20 hours. Data showed an immediate and systematic increase in resistance and decrease in capacitance of DOPC membrane in the electrochemical cell that equilibrates in under 2 hours of bilayer preparation, beyond which the signal remains constant for up to 18 hours. The initial equilibration data (from 0 to 2 h) are not included in the plot for clarity. Fig. 2A and B (grey) shows representative temporal stability data over 2–18 hours for DOPC MSLB showing relative resistance and capacitance after initial equilibration. For peptide binding studies, 1 μM Aβ_{1-42} in its monomeric form (*cf.* fluorescence correlation spectroscopy data in Fig. S4, ESI†) was added to the membrane contact buffer following membrane's electrochemical equilibration, and impedance sampled for at least 18 hours (*i.e.*, within the stability window of pristine membrane). The corresponding relative changes in resistance and capacitance are shown in Fig. 2A and B (orange) respectively. After a modest fluctuation of membrane resistance within 1–2 hours of Aβ_{1-42} incubation (*cf.* the time window from 2–4 hours in Fig. 2A, orange), the resistance remains indistinguishable from that of pristine membrane for at least 10 hours. Beyond 10 hours, resistance starts to decrease. The capacitance, on the other hand, decreases systematically over the full experimental window after exposure to Aβ_{1-42}. This may suggest weak and slow physisorption of Aβ_{1-42} at the membrane over time, but with limited impact on overall membrane organization. Our results are consistent with a previous study in which Aβ_{1-42} monomers were observed to weakly bind to zwitterionic DOPC bilayer.[20] It is worth noting that in the absence of Aβ_{1-42}, a modest decrease in capacitance of the pristine DOPC membrane (grey, Fig. 2B) occurs over the course of 18 h, which may be attributed to the impact of HEPES buffer, which has been reported to cause the membrane to rigidify.[61,79] Nonetheless, the capacitance changes are greater in the presence of Aβ_{1-42}. Decoupling the contributions of both effects is challenging, therefore, to gain more insight, we carried out atomic force microscopy (AFM) studies at a flat mica SLB platform to visualize any nano to submicroscopic changes caused by Aβ_{1-42} to the DOPC membrane within the time range of EIS observations (Fig. 2C). In line with EIS, the membrane remains quite homogeneous in the presence of 1 μM Aβ_{1-42} peptide beyond 10 h. Some modest heterogeneity is evident after 15 h (*cf.* white arrow mark, Fig. 2C, right panel) consistent with the time frame of the EIS resistance decrease.

To confirm that Aβ_{1-42} adsorbs at the DOPC membrane without damaging or porating it, a confocal fluorescence microscopy-based leakage study was carried out on an analogous PDMS cavity array with DOPC MSLBs. Prior to bilayer formation, the cavities were filled with 5 μM pyranine, a fluorophore that is impermeable to the bilayer and thus expected to remain trapped in the cavity while the membrane is intact.[62] This experiment also serves to confirm that the bilayer is effectively spanned across the pore array. Fluorescence imaging was then performed after $\sim$3 h incubation of DOPC MSLB with 1 μM Aβ555 at 20 $\pm$ 1 °C. The reflectance image in Fig. 3A clearly distinguishes between cavities that are filled (dark circular regions) with buffer/pyranine and a small number of cavities that are not filled (marked by an arrow) thus not bilayer sealed (*cf.* arrow, Fig. 3B). However, notably in the case of MSLB over gold support, where the dimension of pores is smaller and bilayer is supported by modification of the intervening top surface with OH terminate SAM, we observed continuous aqueous filling and well spanned membrane across the substrate (Fig. S1B–D, ESI†). The observation of occasional unfilled/unspanned pores in PDMS is attributed to the larger size of these pores ($\sim$2 μm diameter, compared to 1 μm in gold) and to the hydrophobicity of the substrate that can sometimes mitigate against complete aqueous filling where plasma treatment may not have reached all pores. The confocal fluorescence images of a bilayer doped with DOPE-Atto655 (0.05 mol%) at the distal leaflet of the membrane (Fig. 3B) confirms the bilayer is spanned over the buffer/pyranine filled cavities. Fig. 3C shows the fluorescent image collected from Aβ555 (green), and the overlayed (Fig. 3D) image confirms it is weakly associated with the membrane above the pyranine (side on image shown in Fig. S7, ESI†). The pyranine signal (shown in yellow), from the filled pores is clearly visible (Fig. 3D) both from within the pores and is particular intense from the pore walls where the bright emission is attributed to the accumulated signal along the vertical walls of the pores in the confocal z-axis. This is attributed to weak adsorption of the pyranine to

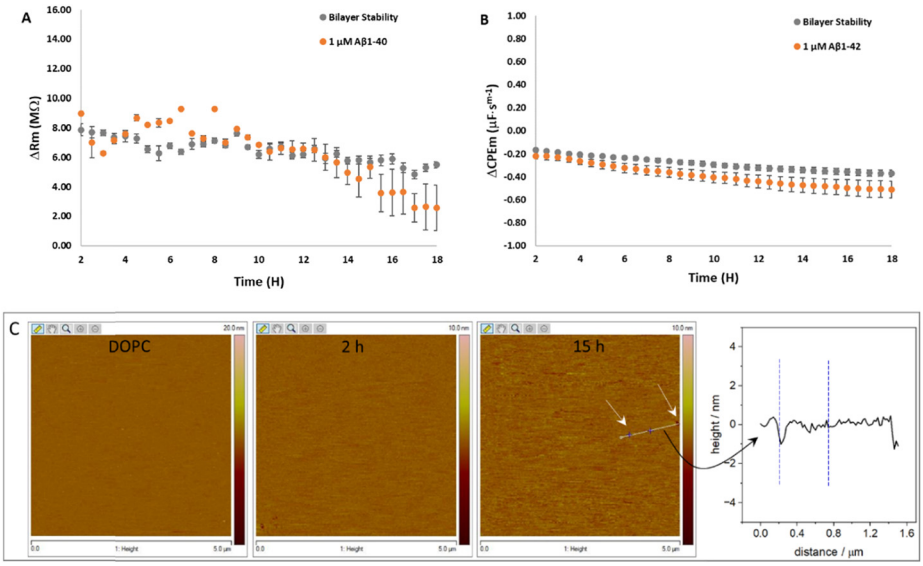

Fig. 2 Top representative temporal electrochemical data from DOPC bilayers suspended in a 1 μm diameter gold cavity array showing the relative change in membrane (A) resistance and (B) capacitance *versus* time before (grey) and after (orange) the addition of $A\beta_{1-42}$(1 μM) in HEPES buffer at pH 7.4 over 20 hours. EIS measurements were performed in HEPES electrolytes (pH 7.4) at 20 °C using gold microcavity suspended bilayer as working electrode, Ag/AgCl (1 M KCl) as reference electrode and Pt coil as counter electrode. Measurements were taken at an AC perturbation amplitude of 10 mV with DC bias potentials 0 V (*vs.* Ag/AgCl), over the frequency range from 0.01 to 10^4 Hz. Equilibration of DOPC lipid bilayer was achieved within 2 hours after bilayer preparation (data from 0–2 h are excluded for clarity), and the impedance change remained constant for over 18 hours. The data recorded are the mean of N = 3 with error bars representing standard error. (C) Topographic tapping mode AFM images (5 μm × 5 μm) of DOPC bilayer without and with 1 μM $A\beta_{1-42}$ at different time intervals. The depression induced by $A\beta_{1-42}$ are indicated by the white arrow in the 15 h panel and the corresponding line profile shown to its right. For both EIS and AFM studies, the bilayer is prepared by the LB-VF method. The AFM are acquired on a freshly cleaved mica and imaged under the HEPES buffer.

the plasma treated, hydroxylated PDMS surface. The propensity for adsorption of pyranine at hydroxylated surfaces has been noted previously at polymer and graphene.[96–98]

After 3 hours incubation with Aβ555, there was no change in bilayer emission image or pyranine emission intensity or any leakage evident of the pyranine, confirming, consistent with EIS and AFM data that the bilayer is intact and not damaged by the amyloid under these conditions.

Effect of $A\beta_{1-42}$ on an asymmetric negatively charged DOPC : DOPS (90 : 10)//DOPC membrane

PS concentrations in plasma membranes range from 5 to 10% (mol/mol) and can reach up to 20 (molar%) in neuronal cell membranes.[40,80] In healthy cells, PS is localized to the cytoplasmic leaflet. When the membrane is damaged, *e.g.* by oxidative stress, the PS translocates to the exterior leaflet, where it serves as an "eat me" signal for cellular apoptosis,[81–85] a hallmark biomarker of AD. Typically Aβ is found in healthy brains at low femto to picomolar levels, but is elevated in AD.[86,87]

Using EIS, we therefore set up an onset monomeric $A\beta_{1-42}$ working concentration in the pico to subnanomolar range at an asymmetric MSLB comprised of DOPC at the proximal leaflet and DOPC : DOPS (90 : 10) at the distal leaflet. This range of Aβ concentration is not expected to lead to oligomer formation, emulating a healthy brain cell.[3,86,88,89] Previously, μM $A\beta_{1-42}$ concentrations have been used to instigate oligomer/fibril formation, especially in zwitterionic membranes or in aqueous solution[55,57,74,90–92] whereas pM-sub nM have been used to mimic oligomer formation when cholesterol and/or charged lipids are present.[50,73] Because Aβ oligomerization is a slower process than its detergent-like behaviour, which is a fast process, EIS was employed to tap the later process. Furthermore, working below the critical micelle concentration of $A\beta_{1-42}$ and incubating for a short period of time (30 minutes) allows us to capture the entire range of concentrations within our overall experimental time window (18 hours) and prevent difficulties that could result in aggregation-induced membrane damage.[93]

Fig. 4A shows the relative resistance changes to an asymmetric DOPC : DOPS (90 : 10)//DOPC membrane on titration of different concentrations of $A\beta_{1-42}$. Fig. 4B shows the corresponding relative capacitance plot. Each data point was collected after 30 minutes of incubation at the designated $A\beta_{1-42}$ concentrations. Over the concentration range 25–200 pM, no change in membrane resistance or capacitance was evident. However, from 400 pM of $A\beta_{1-42}$, the membrane resistance proceeded to decrease, suggesting that oligomerization commences around 400 pM, (notwithstanding the limit of detection in our experimental set-up for detecting oligomerization). Since oligomerization and fibril formation at the bilayer interface is a slow process[94] even at elevated (μM) amyloid concentrations, the decrease in resistance after 30 min incubation is most likely due to partial membrane insertion and the first step in oligomerization. Beyond 800 pM $A\beta_{1-42}$, dramatic decreases in membrane resistance are evident, indicating that significant interaction of $A\beta_{1-42}$ with the anionic membrane. The bilayer capacitance remains unchanged across the range 400 to 800 pM

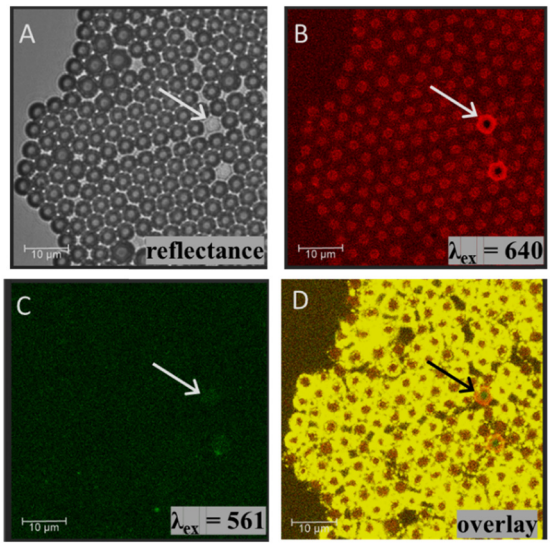

Fig. 3 (A) Reflectance image of DOPC MSLB spanning over pyranine containing buffer filled PDMS substrate. The dark grey circular features in the reflectance image are the cavities that filled with buffer. The occasional unfilled cavity is easily distinguished in reflectance, as indicated by an arrow and appear as bright spots. (B) A confocal fluorescence image of -Atto655 labelled DOPC MSLB across the same region as the reflectance image, showing the bilayer spanned over pyranine/buffer filled cavities. The pores where buffer failed to fill or where bilayer fail to span are also clear, as in these unfilled pores, the intense emission from the pore edges are due to emission from along vertical walls of the pores captured in the confocal volume due to the lipid lining the pore. (C) A confocal fluorescence image of the DOPC MSLB in contact with Aβ555 after 3 hours of incubation, showing homogenous weak emission from Aβ555 at the bilayer. The overlayed image of panels B (red) and C (green) along with signal obtained from pyranine (yellow) are shown in panel D. The emission is evident from the pores but is exceptionally bright at the pore walls due to weak adsorption of the pyranine at the hydroxylated PDMS. The red channel in panel B is the emission from DOPE-Atto655 (0.05 mol%) which was doped at the upper leaflet of DOPC bilayer with excitation wavelength, λ_{ex} = 640 nm and detection window 650–780 nm; the yellow channel is the emission from pyranine (5 μM) with excitation at 405 nm and detection window 440–560 nm; and the green channel is the emission from Aβ555 (1 μM) with excitation at 561 nm and detection window 570–630 nm. In each panel, the scale bar was 10 μm.

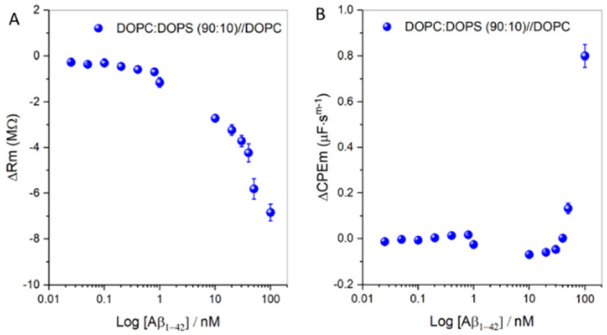

Fig. 4 Concentration-dependent titration curve for the effect of $A\beta_{1-42}$ on the impedance of the DOPC : DOPS (90 : 10) asymmetric membrane. (A) Represents the relative resistance change, whilst (B) represents the capacitance change of the membrane after incubation with different concentrations of $A\beta_{1-42}$. A 30 minute incubation period following membrane equilibration was established for each concentration of $A\beta_{1-42}$, followed by the addition of next concentration. Any change in membrane impedance caused by $A\beta_{1-42}$ is normalized with respect to the pristine equilibrated membrane impedance (before any amyloid addition). The results shown are the averages of at least three independent experiments ($N \geq 3$).

of $A\beta_{1-42}$, but not to 1 nM. Together, the data suggests some insertion of monomeric $A\beta_{1-42}$ into the membrane, leading to increased membrane admittance without changes to membrane thickness. 10 nM $A\beta_{1-42}$ decreases resistance to ~2.7 MΩ and capacitance modestly, indicating enhanced admittance and bilayer thickness. Above 10 nM $A\beta_{1-42}$, membrane resistance drops as capacitance increases indicating membrane damage. The data reveal a significant change in bilayer impedance at higher $A\beta_{1-42}$ concentrations, with the capacitance increasing to ~0.8 μF s^{m-1} and the resistance decreasing to −6.84 MΩ, suggestive of pore formation and likely indicating that oligomerization of amyloid is underway from 400 pM. Given the dynamic and complex nature of the $A\beta_{1-42}$-membrane interaction, extracting association data from the resistance curve was not possible as we cannot assume that the process had reached equilibrium at the 30 minute time point at which the data was collected. Therefore, to dynamically follow the oligomerization process at the DOPC:DOPS asymmetric membrane, we extended the incubation period of $A\beta_{1-42}$ with membrane at different fixed concentrations of 100 nM, 1 μM and 2 μM.

Fig. 5A and B show representative plots of relative change to resistance and capacitance of an asymmetric DOPC : DOPS (90 : 10) membrane over time. As noted before, the initial 2 hours equilibration window is excluded from the plot. The data (Fig. 5A and B) show that the membrane is stable for 18 hours, similar to the pristine zwitterionic DOPC bilayer, (*cf.* Fig. 2) defining the experimental window.

For all three $A\beta_{1-42}$ concentrations (100 nM, 1 μM and 2 μM), the resistance decreased considerably over the first several hours as shown in Fig. 5C, E and G. The magnitude of the change suggests membrane damage; loss of lipid or possibly pore formation, which is consistent with the carpet model.[22–24,95] Such a large resistance drop was not observed at the pristine DOPC (without DOPS) membrane, implying that the anionic charge of the DOPC : DOPS facilitates the effect. This is consistent with previous observations that PS in the bilayer catalyses $A\beta_{1-42}$ aggregation on the membrane.[37,41] Notably for 100 nM $A\beta_{1-42}$, the membrane resistance (Fig. 5C) continued to decrease and then equilibrated. The corresponding capacitance (Fig. 5D) also decreased, and the extent of decrease remained large when compared to the capacitance without $A\beta_{1-42}$. A modest decrease in pristine membrane capacitance (0 nM $A\beta_{1-42}$) may be due to the HEPES buffer as observed in our earlier study.[61]

Increasing amyloid concentrations over 100 nM resulted in resistance increase (recovery) after 7 hours of decreasing resistance in 1 μM $A\beta_{1-42}$; where final membrane resistance eventually surpassed the initial membrane resistance (Fig. 5E). We speculate that this is due to adhesion of $A\beta_{1-42}$ oligomers across the bilayer interface, which is supported by the AFM data below. The corresponding membrane capacitance (Fig. 5F) decreases, also indicating membrane thickening, but the extent

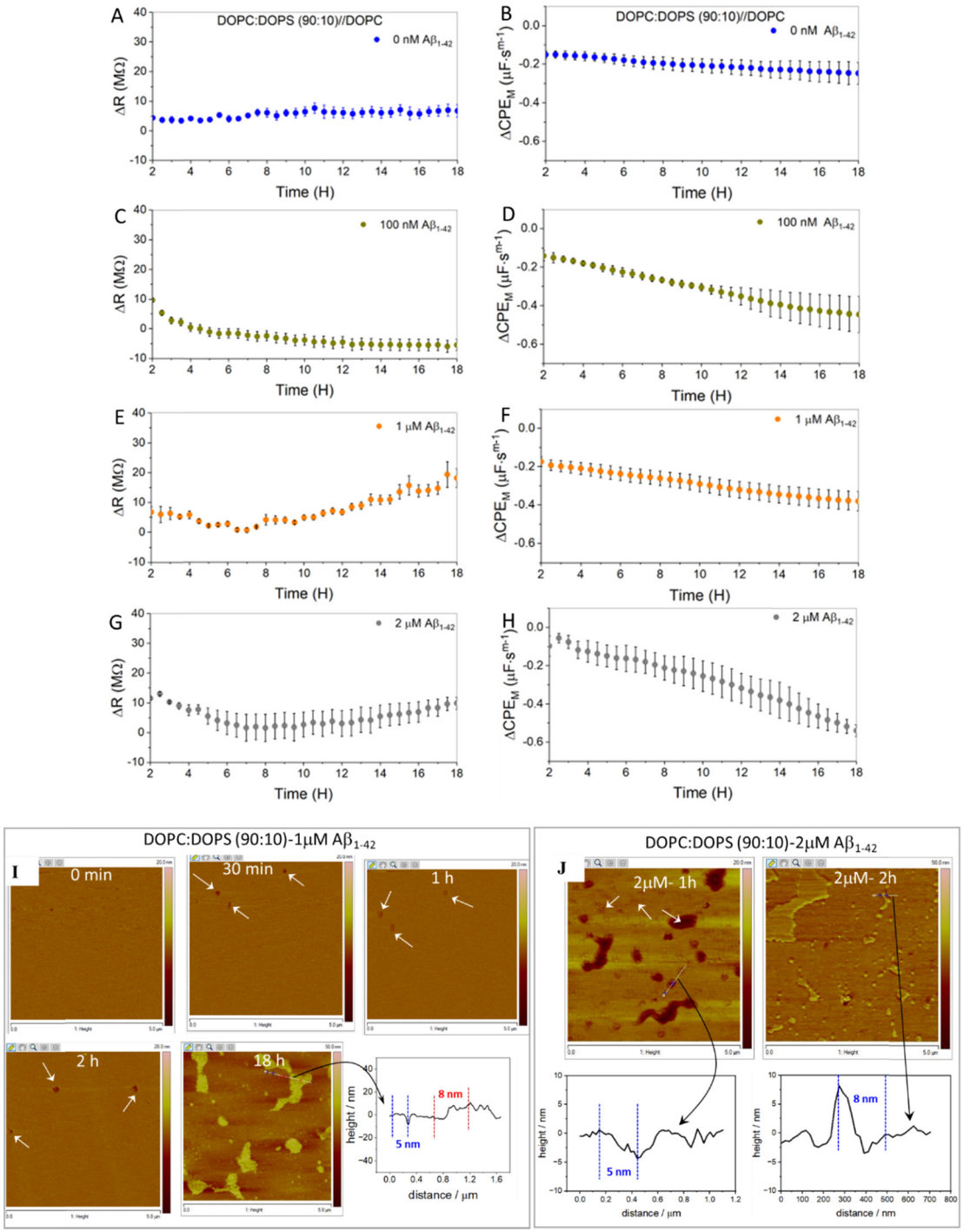

Fig. 5 Temporal evolution of changes in relative resistance and capacitance of DOPC : DOPS (90 : 10)//DOPC asymmetric bilayer without and in presence of different concentrations of $A\beta_{1-42}$. In the absence of $A\beta_{1-42}$ the relative change in (A) resistance and (B) capacitance showing the stability of an asymmetric DOPC : DOPS (90 : 10) MSLB. In presence of 100 nM $A\beta_{1-42}$ real time temporal evolution of (C) resistance and (D) capacitance changes are shown. (E and F) Illustrates the resistance and capacitance change respectively with incubation of 1 μM $A\beta_{1-42}$. The corresponding resistance and capacitance change in presence of 2 μM $A\beta_{1-42}$ are shown in panel (G) and (H) respectively. For EIS measurements, all samples were in contact with HEPES buffer at pH 7.4. In all the panels A–H, the experimental data is presented, ranging 2 to 18 hours. The error bars represent the standard error across the samples (N = 3). Temporal evolution of topographic AFM images of asymmetric DOPC : DOPS (90 : 10) bilayer deposited on mica before and after incubation with (I) 1 μM $A\beta_{1-42}$ and (J) 2 μM $A\beta_{1-42}$, as well as height profile analysis. In panel I and J, the image size was 5 μm × 5 μm. $A\beta_{1-42}$ induced lipid disruption is indicated by the white arrow in panels I and J. The line profile analyses plots corresponding to the image are indicated by black arrow and was taken from a cross-section in the region of interest, marked in white solid line in the respective images. All images are acquired under liquid and the membrane was prepared *via* LB-VF method.

of change and kinetics remain low when compared to 100 nM $A\beta_{1-42}$. This is attributed to concomitant pore-formation followed by oligomer formation at higher $A\beta_{1-42}$ concentrations. Notably, at 2 μM $A\beta_{1-42}$, the increasing (recovering) resistance (at 18 h) does not surpass the initial membrane resistance (at 2 h time point); this is attributed to competing effects of layer formation and concomitant damage inflicted on the membrane. Although there was a clear decrease in capacitance overall, on initial addition of 2 μM $A\beta_{1-42}$ it was observed to increase for the first 1–2 h before progressively declining over the following 18 h (*cf.* Fig. 5H). This initial increase in capacitance could be due to the removal of lipids as a result of the high concentration of $A\beta_{1-42}$ (2 μM), possibly a detergent-like effect.

Irrespective of the concentration of $A\beta_{1-42}$ used, our data suggests carpet model behaviour, especially within the incubation widow of 1–7 hours. However, the resistance increase (recovery) over longer length-scales, after reaching a minimum, deviates from the carpet model (Fig. 5E and F). Chang *et al.*[95] noticed this ambiguity when analysing antimicrobial peptide (AMPs) interactions with model membrane, using EIS within a 25 minutes time span and termed it as carpet ''raft''. The $A\beta_{1-42}$ aggregate formation is a very slow process that differs from AMPs, and our data captures this longer-scale process. As pointed out earlier by Chang *et al.*[95] because the carpet model does not precisely explain how peptide rafts destabilize the membrane, our EIS results (particularly in the case of 1 and 2 μM $A\beta_{1-42}$) cannot definitively rule out or agree with the carpet model. Membrane instability and aggregation may occur in nanoscale regimes within the bilayer, that do not lead to full destruction, given we see detectable resistance during incubation. Resistance increase could be linked to network-like, possibly stacked $A\beta_{1-42}$ layers that forms across the bilayer surface. To investigate this further we performed AFM studies to visualize any structures forming at the membrane directly.

Fig. 5I shows AFM images of the DOPC:DOPS SLB membrane on cleaved mica before, and at different time intervals following, incubation with 1 μM $A\beta_{1-42}$. Before addition of $A\beta_{1-42}$, the DOPC:DOPS membrane is quite homogeneous (Fig. 5I, 0 min). Within 30 minutes of incubation with 1 μM $A\beta_{1-42}$, nanoscale depressions (see arrow in Fig. 5I) appear on the bilayer surface. The density and dimensions of the features grow over time until 4–6 h (for reference, the impact of $A\beta_{1-42}$ at different time intervals such as 0.5, 1 and 2 h data are shown in Fig. 5I). This observation is strongly consistent with EIS data, which show a decrease in membrane resistance (Fig. 5E) over this window. The $A\beta_{1-42}$ oligomer is stacked in patches and distributed heterogeneously over the membrane's surface when observed at 18 hours. The micron-scale patches, attributed to network-like layered aggregates of $A\beta_{1-42}$ oligomers, protrude from the bilayer surface at a height of ~8–10 nm, as shown in the bottom right panel of Fig. 5I. This is consistent with a report by D'Ursi *et al.* for AFM study on $A\beta_{25-35}$ interaction with bilayer membrane.[92] The $A\beta_{1-42}$ oligomer network formation commences after 6 hours of incubation (data not shown) and continues to grow, which is again strongly consistent with our electrochemical data, in which membrane resistance increased and capacitance decreased over the same time period.

Within 1 hour of incubating 2 μM $A\beta_{1-42}$ at the membrane, dramatic changes in the AFM of the DOPC:DOPS membrane were evident, with extensive pore formation and membrane damage (*cf.* Fig. 5J). At this concentration, $A\beta_{1-42}$ seems to behave like a detergent, removing patches of membrane from the bilayer surface and creating pores with dimensions of (10–30 nm diameter). The regions where bilayer patches have been completely removed appear dark in the images (Fig. 5J, left). The line profile analyses (bottom left, in panel J) distinguish two regions: areas of lipid removal, with a height difference between mica and the top surface membrane of 5 nm, consistent with the known thickness of DOPC membrane, and circular pore like regimes with a depression of 1.6 nm from the bilayer surface. At the center of these circular features, globular $A\beta_{1-42}$ aggregates with lateral dimensions of ~4–6 nm can be distinguished, likely the oligomeric seed. Although this observation correlates with EIS data, considering the significant change in morphology, one might expect the extent of resistance drop and capacitance rise during the initial incubation time-window to be substantially higher. One plausible explanation for this variation relates to the experimental incubation conditions, where in AFM, the incubation was carried out a horizontally oriented substrate in a ~200 μL liquid cell *versus* a vertically oriented substrate in a 5 mL volume for EIS measurement. Although absolute $A\beta_{1-42}$ concentrations were the same, the effects of gravity and low volume in the AFM measurement cell, is likely to lead to higher local concentration of peptide incident at the membrane surface in the AFM experiment which may accelerate the process compared to the EIS set-up. Nevertheless, the image acquired at 18 hours of incubation, shows heterogeneous large scale $A\beta_{1-42}$ aggregates had developed and covered up to ~20% of the bilayer surface. Fig. 5J shows a representative image of the layered as well as globular aggregates covering the bilayer surface, that protrude at a height of ~8 nm (right panel, Fig. 5J). These AFM results, which were highly reproducible across multiple replicates, explain the resistance increase (recovery) observed in EIS in terms of oligomeric growth and the associated drop in capacitance, which causes the formation of a peptide layer at the membrane interface, leading to membrane thickening. Overall, the data agree well with the hypothesized theory illustrated in Fig. 1 that the interaction of Aβ at the negatively charged membrane follows initial binding, pore formation, lipid dissolution, and growth in oligomer formation, and also provides additional insights towards the concentration dependence and the time scale of Aβ oligomer formation.

To further confirm pore formation by 1 μM $A\beta_{1-42}$ on the DOPC:DOPS membrane and its influence on bilayer integrity, confocal fluorescence imaging was carried out. Fig. 6 shows the impact of 1 μM Aβ555 after 3 hours of incubation on an asymmetric DOPC : DOPS (90 : 10) membrane suspended over PDMS cavity array. Fig. 6A shows the confocal image obtained from DOPC:DOPS MSLB labeled with DOPE-Atto655. The association of Aβ555 (green emission) to the membrane is shown in

Fig. 6B. As expected, pore-like features could not be distinguished due to the diffraction limit of optical microscopy. However, it is clear that after 3 hours of incubation with 1 μM Aβ555 there is extensive loss of the pyranine from the pores (Fig. 6C). This behaviour contrasts sharply with images collected under identical conditions in Fig. 3C at the DOPC-only membrane, where following Aβ555 incubation, pyranine remained trapped by the intact membrane, and brightly emissive from the cavity walls. From the overlayed images of DOPC (Fig. 3D) and DOPC:DOPS (Fig. 6D) after Aβ incubation it is clear that the pyranine escapes from the cavity attributed to leakage due to poration of the DOPC:DOPS membrane.

Furthermore, according to the hypothesized mechanism described in Fig. 1, when Aβ self-assembly leads to larger scale oligomers/fibrils, they are released from the membrane into the contact solution.[55,99,100] To explore this, the contacting electrolyte solution from the impedance experiments after 24 hours of Aβ incubation with the membrane were collected and studied *via* UV/Vis and fluorescence, following treatment with thioflavin T (Tht). Tht is a fluorescent probe is known to bind specifically to amyloid fibrils but not to amyloid monomers. In the absence of amyloid, the absorbance of Tht alone in HEPES buffer was 411.5 nm, and the emission was 480 nm. When Tht is added to the electrolyte, along with the emission peak at 480 nm, another peak at 510 nm appears (Fig. S5, ESI†) attributed to the Tht bound to the Aβ fibrils/aggregates,[101,102] indicating that fibrils/oligomers are indeed released from the membrane into the contact solution after 24 hours incubation of 1 μM $Aβ_{1-42}$ with asymmetric DOPC : DOPS (90 : 10)//DOPC membrane.

Effects of DOPS concentration within asymmetric DOPC:DOPS//DOPC membrane

Next we evaluated the impact of DOPS content on oligomerization, first by applying 1 μM $Aβ_{1-42}$ to a MSLB containing 5 mol% DOPS in the distal leaflet (Fig. 7A and B, orange). The resistance decreased over time (Fig. 7A, orange), with no evidence of increase resistance (recovery) as observed earlier at 10 mol% DOPS concentration (*vide infra*, *cf.* Fig. 5E). Simultaneously, the membrane capacitance increased systematically with time (Fig. 7B, orange), indicating membrane thinning or pore formation. Consistent with the EIS observation, AFM images of 5 mol% DOPS containing membrane, as shown in Fig. S8 (ESI†), reveal pores but no aggregation or layers form, even after prolonged incubation with 1 μM $Aβ_{1-42}$.

Incubation of 2 μM $Aβ_{1-42}$ with a membrane containing 5 mol% DOPS, on the other hand, shows resistance decreases over 3–4 h that subsequently recovers (grey, Fig. 7A). Simultaneously, membrane capacitance decreases modestly after 4 h (grey, Fig. 7B), indicating thickening of membrane/layer formation. The resistance and capacitance profiles are reminiscent of those for 1 μM $Aβ_{1-42}$ at

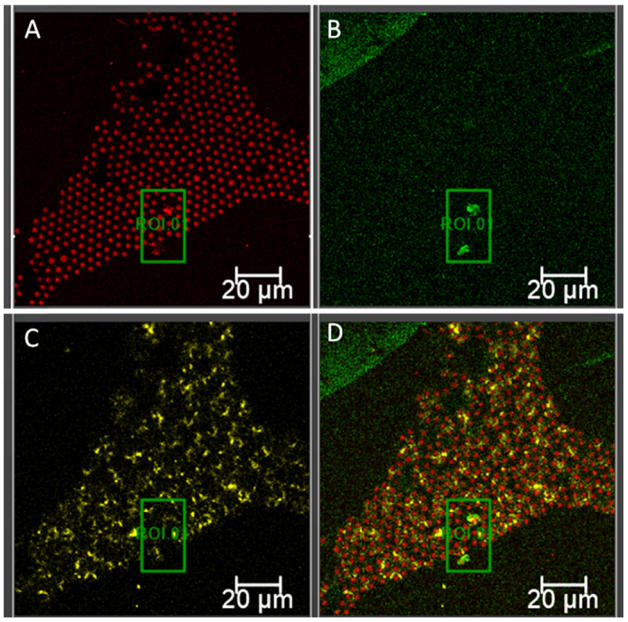

Fig. 6 Confocal fluorescence microscopy images of an asymmetric DOPC : DOPS (90 : 10) bilayer spanning a pyranine (5 μM) filled PDMS microcavity array after 3 hours of incubation with 1 μM Aβ555. Confocal image of DOPC:DOPS MSLB displaying the fluorescence signal of fluorescently labelled (A) DOPE-Atto655 excited at 640 nm with detection window 650–780 nm; (B) Aβ555 excited at 561 nm with a detection window of 570–630 nm; and (C) pyranine fluorescence image obtained with an excitation wavelength of 405 nm and a detection window of 440–560 nm showed dramatic loss of pyranine emission signal. (D) Overlayed fluorescence images displaying the association of Aβ555 with the bilayer surface, resulting leaky pyranine signal and Aβ555 aggregates as indicated by region of interest, ROI 0. The scale bar in each panel measures 20 μm.

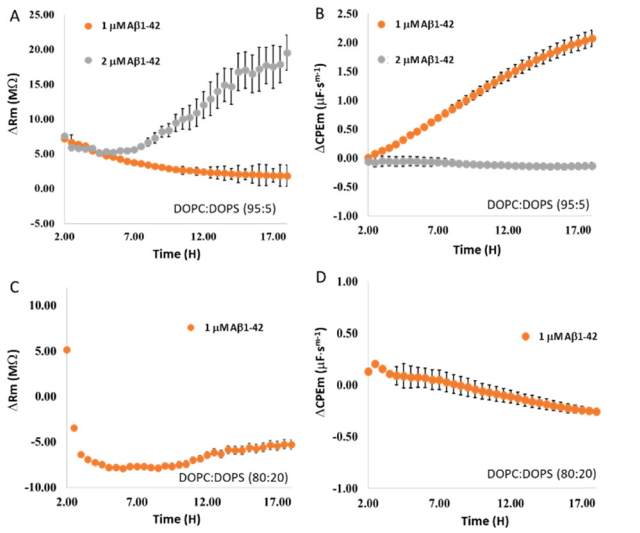

Fig. 7 Temporal changes in relative (A) resistance and (B) capacitance of a DOPC : DOPS (95 : 5)//DOPC membrane following addition of 1 μM (orange) and 2 μM (grey) $Aβ_{1-42}$. All EIS measurements were performed in HEPES buffer at pH 7.4. After 1.5 hours of membrane equilibration (*cf.* Fig. S6, ESI†), designated concentration of $Aβ_{1-42}$ was added. Panels C and D show the relative temporal changes in resistance and capacitance of the DOPC : DOPS (80 : 20)//DOPC asymmetric bilayer membrane (orange) after the addition of 1 μM $Aβ_{1-42}$. Prior to the addition of $Aβ_{1-42}$, membrane's stability was established, and it was found that beyond 1.5 hours, the membrane resistance and capacitance remained unchanged, establishing the time point for $Aβ_{1-42}$ incubation. All measurements are performed in triplicates (N = 3), and the error bars reflect standard error.

10 mol% DOPS containing membrane (*vide infra*), indicating, that when DOPS content is reduced, more $A\beta_{1-42}$ is required to induce oligomerization and form layered aggregates.

At membranes containing 20 mol% of DOPS, 1 μM $A\beta_{1-42}$ elicited a dramatic decrease in resistance (Fig. 7C) within 1 h of incubation and remained steady over ~9–10 h. Resistance began to recover modestly after this time point. Simultaneously, the membrane capacitance increased modestly within 1 h, then systematically decreased (Fig. 7D), suggesting the formation of layered aggregates. Overall, the data indicate that the rate and extent of oligomer formation are affected by the concentrations of both DOPS and $A\beta_{1-42}$. When the membrane concentration of DOPS is decreased, a higher concentration of $A\beta_{1-42}$ is required for the formation of oligomer. Combined, data across 18 hours indicate that at a fixed concentration of 1 μM $A\beta_{1-42}$ and variable DOPS content, pore formation is only predominant when 5 mol% DOPS is present (as seen by a systematic rise in capacitance *versus* time, Fig. 7B (orange)), without concomitant fibril/oligomer formation; whereas when DOPS content is increased to 10 or 20 mol%, a modest capacitance rise is evident at within 1–2 h (Fig. 7D and 5F), but overall remains decreased beyond this time window.

Effects of $A\beta_{1-42}$ on an asymmetric DOPC//DOPC:DOPS (90 : 10) membrane on optothermal damage

Varying the concentration of DOPS (20, 10 and 5 mol%) in the proximal leaflet in a bilayer with only DOPC present in the exterior leaflet, we then attempted to mimic discrete areas of PS translocation that might occur in lipid damage due to oxidative stress and apoptosis of neurons associated with aging of the brain. This was accomplished by optothermally damaging the membrane with a laser to initiate DOPS transversal diffusion as reported prevously.[61] In the absence of photodamage, DOPC//DOPC : DOPS (90 : 10) bilayers were found to be stable for at least 10 hours, as shown previously by assessing transversal diffusion of DOPS *via* annexin binding.[61] After initial equilibration, the MSLB was irradiated for 10 seconds with a 405 nm laser at 3.12 mW power. As reported previously, for all DOPS concentrations used in this study, irradiation led to a decrease in resistance confirming optothermal induced increase in membrane admittance associated with bilayer annealing and increased local fluidity.[62] Correspondingly, the capacitance does not change significantly during this process, indicating that the membrane was not seriously damaged by the laser. When 20 mol% DOPS was present at the proximal leaflet, the resistance reduced considerably when 1 μM $A\beta_{1-42}$ was added following photothermal damage. Although, the drop in resistance is significant (Fig. 8A), the extent of decrease in resistance and the associated kinetics remains low when compared to the case when 20 mol% DOPS was present on the distal leaflet (Fig. 7C, *vide infra*).

Within 1–2 hours of $A\beta_{1-42}$ incubation following laser damage, the capacitance increases, but then systematically decreases over 18 hours. The overall magnitude of decrease in capacitance remains modest when compared to when 20 mol% DOPS is included at distal leaflet. Because optothermally induced DOPS transverse migration from the lower to upper leaflet results in much lower DOPS concentration at the exterior leaflet, $A\beta_{1-42}$ binding is expected to be significantly lower. When 10 mol% DOPS is present at the proximal leaflet, laser damage induced a modest increase in overall resistance, although the resistance change fluctuated over this incubation window and this

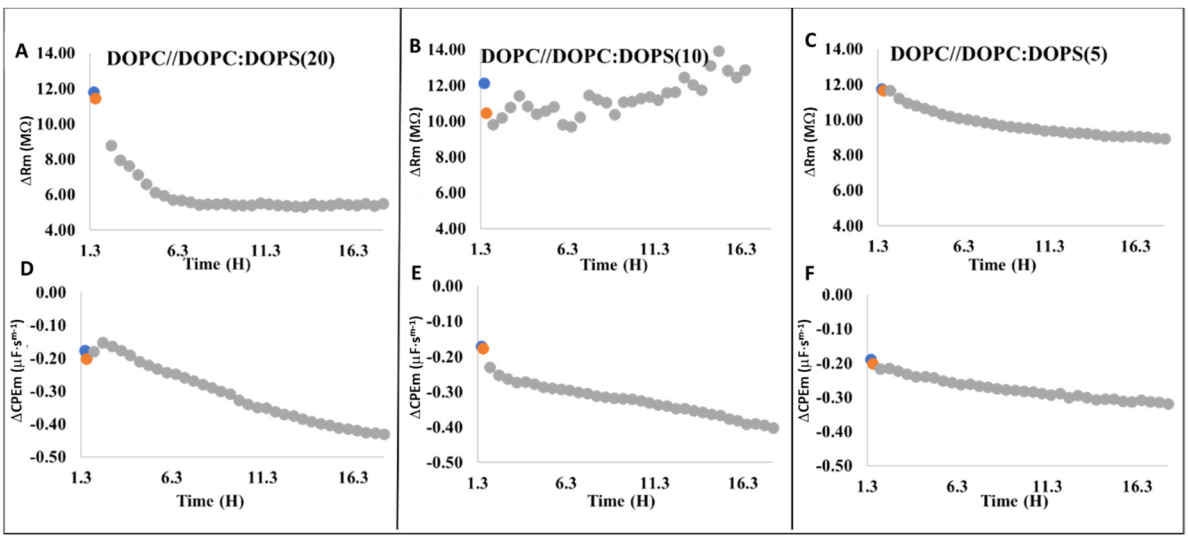

Fig. 8 Representative relative resistance (A–C) and relative capacitance (D–F) changes as a result of 1 μM $A\beta_{1-42}$ binding at different DOPS containing asymmetric DOPC//DOPC : DOPS MSLBs: (A and D) DOPC//DOPC : DOPS (80 : 20); (B and E) DOPC//DOPC : DOPS (90 : 10); and (C and F) DOPC// DOPC : DOPS (95 : 5). After photodamaging the MSLBs for 10 s with a 405 nm laser, $A\beta_{1-42}$ was introduced into each type of membrane. In each panel, blue circles represent the electrochemically equilibrated membrane's resistance and capacitance, stability time point, whereas orange circle represent the corresponding data points following photodamage and defines the time point when $A\beta_{1-42}$ was introduced to the cell. Each panel's grey circles represent the temporal evolution of membrane resistance and capacitance after addition of 1 μM $A\beta_{1-42}$. All data points are the mean of N = 3, and error bars have been eliminated for clarity.

response was reproducible across multiple (N = 3) independently prepared substrates (Fig. 8B). This is surprising as we did not detect this behavior in any other type of membrane or at different concentrations of $A\beta_{1-42}$. However, the trend of decreasing capacitance persisted (Fig. 8E). We speculate that transient $A\beta_{1-42}$ interactions with the DOPS exposed at the outer leaflet may explain this dynamic interaction and tentatively attributed the observed electrochemical changes to competing effects of membrane damage/pore formation and rate of $A\beta_{1-42}$ aggregation. In contrast to 20 and 10 mol%, when 5 mol% DOPS was present at the proximal leaflet of the membrane after photothermally initiation, a slow decrease of both membrane resistance (Fig. 8C) and capacitance (Fig. 8F) was observed. Overall, the data revealed that during optothermal damage, there is a pool of local DOPS content at the area of laser focus due to fast flip-flop of DOPS, which may potentially seed and plays a catalytic role in amyloid oligomers formation causing membrane damage. Under identical conditions, when no laser irradiation was performed, DOPS remain at the inner leaflet and impedance changes were comparable to that of DOPC only membrane (data not shown). It is worth noting that none of the optothermally treated DOPC// DOPC:DOPS membranes showed evidence of any large scale oligomerization, as no recovery in resistance is evident.

Conclusions

Microcavity, and mica supported lipid bilayers comprised of DOPC-only and, asymmetric bilayers composed of (external// interior leaflet) DOPC:DOPS//DOPC (with varying DOPS concentrations on the exterior leaflet), and DOPC//DOPC:DOPS (with varying DOPS concentrations on the interior leaflet) were evaluated for $A\beta_{1-42}$ binding and aggregation using electrochemical impedance spectroscopy, AFM and confocal fluorescence microscopy.

At pristine DOPC membrane, $A\beta_{1-42}$ appears to adsorb at the zwitterionic membrane interface, without aggregation even at 1 μM of peptide. Using a membrane integrity test with pyranine, we observed that the DOPC membranes remained intact and impermeable to the probe in the presence of $A\beta_{1-42}$.

The presence of anionic DOPS in the membrane dramatically alters the way $A\beta_{1-42}$ interacts with the membrane. Oligomerization of $A\beta_{1-42}$ monomer was observed by EIS and AFM, and confocal microscopy, when DOPS was exposed to the outer membrane leaflet. Over time, there was evidence of both pore formation (at short time frames) and oligomerization-with extensive membrane-oligomer multilayer binding and $A\beta_{1-42}$ fibril formation (3 to 18 hours). The extent of oligomerization and membrane damage depended on the concentrations of DOPS in the membrane and $A\beta_{1-42}$ in the contacting solution. The peptide aggregation was accelerated at the highest $A\beta_{1-42}$ and DOPS concentrations, as expected, and the extent of membrane damage increased with $A\beta_{1-42}$ concentration. The data suggested that all of the hypothesized membrane $A\beta_{1-42}$ interactions (pore formation, dissolution and carpet effect) occur, but the outcome is dependent on the concentrations of both $A\beta_{1-42}$ and DOPS.

In a simple model of DOPS translocation that occurs in damaged neuronal membranes associated with *e.g.*, oxidative stress and apoptosis, asymmetric membranes with DOPS localized to the lower leaflet were prepared, and DOPS lipid transversal migration was instigated optothermally to create local regions of high concentration of DOPS. Our data indicated that higher concentrations of DOPS (>10 mol%) at the lower leaflet migration of anionic lipids can seed $A\beta_{1-42}$ aggregation where DOPS appears to have a catalytic effect on Aβ oligomerization.

Author contributions

T. E. K. designed and directed the research. J. R. and N. K. S. performed the experiment and analysed the data. J. R, N. K. S. and T. E. K. wrote the manuscript.

Conflicts of interest

There are no conflicts to declare.

Acknowledgements

This material is based upon work supported by Science Foundation Ireland under Grant No. [14/IA/2488], [19/FFP/6428] and [12/RC/2276_P2]. The National Biophotonics and Imaging Platform, Ireland, funded by the Irish Government's Programme for Research in Third Level Institutions, Cycle 4 and 5, Ireland's EU Structural Funds Programmes 2007–2013 and to Irish research council, are gratefully acknowledged for funding under project GOIPG/2020/589.

Notes and references

1 C. A. Ross and M. A. Poirier, *Nat. Med.*, 2004, **10**, S10–S17.
2 J. Näslund, A. Schierhorn, U. Hellman, L. Lannfelt, A. D. Roses, L. O. Tjernberg, J. Silberring, S. E. Gandy, B. Winblad and P. Greengard, *Proc. Natl. Acad. Sci. U. S. A.*, 1994, **91**, 8378–8382.
3 C.-C. Chang, E. Edwald, S. Veatch, D. G. Steel and A. Gafni, *Biochim. Biophys. Acta, Biomembr.*, 2018, **1860**, 1616–1624.
4 K. A. Bruggink, W. Jongbloed, E. A. L. M. Biemans, R. Veerhuis, J. A. H. R. Claassen, H. B. Kuiperij and M. M. Verbeek, *Anal. Biochem.*, 2013, **433**, 112–120.
5 K. H. Ashe, *Alzheimer's Dement.*, 2020, **16**, 1561–1567.
6 C. G. Glabe, *J. Biol. Chem.*, 2008, **283**, 29639–29643.
7 K. L. Viola and W. L. Klein, *Acta Neuropathol.*, 2015, **129**, 183–206.
8 E. N. Cline, M. A. Bicca, K. L. Viola and W. L. Klein, *J. Alzheimer's Dis.*, 2018, **64**, S567–S610.
9 N. P. Cook and A. A. Martí, *ACS Chem. Neurosci.*, 2012, **3**, 896–899.
10 E. Cerasoli, M. G. Ryadnov and B. M. Austen, *Front. Chem.*, 2015, **3**, 17.

11 C. G. Glabe, *Neurobiol. Aging*, 2006, **27**, 570–575.
12 E. Aoraha, J. Candreva and J. R. Kim, *Mol. BioSyst.*, 2015, **11**, 2281–2289.
13 M. Mapstone, A. K. Cheema, M. S. Fiandaca, X. Zhong, T. R. Mhyre, L. H. MacArthur, W. J. Hall, S. G. Fisher, D. R. Peterson, J. M. Haley, M. D. Nazar, S. A. Rich, D. J. Berlau, C. B. Peltz, M. T. Tan, C. H. Kawas and H. J. Federoff, *Nat. Med.*, 2014, **20**, 415–418.
14 B. H. Monien, L. G. Apostolova and G. Bitan, *Expert Rev. Neurother.*, 2006, **6**, 1293–1306.
15 J. V. Rushworth and N. M. Hooper, *J. Alzheimer's Dis.*, 2011, **2011**, 1–14.
16 E. Drolle, A. Negoda, K. Hammond, E. Pavlov and Z. Leonenko, *PLoS One*, 2017, **12**, e0182194.
17 M. Ahmed, J. Davis, D. Aucoin, T. Sato, S. Ahuja, S. Aimoto, J. I. Elliott, W. E. Van Nostrand and S. O. Smith, *Nat. Struct. Mol. Biol.*, 2010, **17**, 561–567.
18 D. Mrdenovic, I. S. Pieta, R. Nowakowski, W. Kutner, J. Lipkowski and P. Pieta, *Int. J. Biol. Macromol.*, 2022, **200**, 520–531.
19 H. H. Jarosz-Griffiths, E. Noble, J. V. Rushworth and N. M. Hooper, *J. Biol. Chem.*, 2016, **291**, 3174–3183.
20 D. J. Lindberg, E. Wesén, J. Björkeroth, S. Rocha and E. K. Esbjörner, *Biochim. Biophys. Acta, Biomembr.*, 2017, **1859**, 1921–1929.
21 L. Puglielli, R. E. Tanzi and D. M. Kovacs, *Nat. Neurosci.*, 2003, **6**, 345–351.
22 D. C. Bode, M. Freeley, J. Nield, M. Palma and J. H. Viles, *J. Biol. Chem.*, 2019, **294**, 7566–7572.
23 J. W. Um, H. B. Nygaard, J. K. Heiss, M. A. Kostylev, M. Stagi, A. Vortmeyer, T. Wisniewski, E. C. Gunther and S. M. Strittmatter, *Nat. Neurosci.*, 2012, **15**, 1227–1235.
24 G. D'Errico, G. Vitiello, O. Ortona, A. Tedeschi, A. Ramunno and A. M. D'Ursi, *Biochim. Biophys. Acta, Biomembr.*, 2008, **1778**, 2710–2716.
25 X. Yu, Q. Wang, Q. Pan, F. Zhou and J. Zheng, *Phys. Chem. Chem. Phys.*, 2013, **15**, 8878.
26 A. Khondker, R. Alsop and M. Rheinstädter, *Membranes*, 2017, **7**, 49.
27 C. Haass and D. J. Selkoe, *Nat. Rev. Mol. Cell Biol.*, 2007, **8**, 101–112.
28 A. Aguzzi and T. O'Connor, *Nat. Rev. Drug Discovery*, 2010, **9**, 237–248.
29 S. Micelli, D. Meleleo, V. Picciarelli and E. Gallucci, *Biophys. J.*, 2004, **86**, 2231–2237.
30 C. Emre, K. V. Do, B. Jun, E. Hjorth, S. G. Alcalde, M.-A. I. Kautzmann, W. C. Gordon, P. Nilsson, N. G. Bazan and M. Schultzberg, *Acta Neuropathol. Commun.*, 2021, **9**, 116.
31 V. E. Kagan, B. Gleiss, Y. Y. Tyurina, V. A. Tyurin, C. Elenström-Magnusson, S.-X. Liu, F. B. Serinkan, A. Arroyo, J. Chandra, S. Orrenius and B. Fadeel, *J. Immunol.*, 2002, **169**, 487–499.
32 M. L. Bader Lange, G. Cenini, M. Piroddi, H. Mohmmad Abdul, R. Sultana, F. Galli, M. Memo and D. A. Butterfield, *Neurobiol. Dis.*, 2008, **29**, 456–464.
33 M.-A. Sani, J. D. Gehman and F. Separovic, *FEBS Lett.*, 2011, **585**, 749–754.
34 K. Matsuzaki, *Biochim. Biophys. Acta, Biomembr.*, 2007, **1768**, 1935–1942.
35 M. del Mar Martinez-Senac, J. Villalain and J. C. Gomez-Fernandez, *Eur. J. Biochem.*, 1999, **265**, 744–753.
36 E. Maltseva and G. Brezesinski, *ChemPhysChem*, 2004, **5**, 1185–1190.
37 H. Ahyayauch, M. Raab, J. V. Busto, N. Andraka, J.-L. R. Arrondo, M. Masserini, I. Tvaroska and F. M. Goñi, *Biophys. J.*, 2012, **103**, 453–463.
38 E. Terzi, G. Hölzemann and J. Seelig, *J. Mol. Biol.*, 1995, **252**, 633–642.
39 C. Wu, M. M. Murray, S. L. Bernstein, M. M. Condron, G. Bitan, J.-E. Shea and M. T. Bowers, *J. Mol. Biol.*, 2009, **387**, 492–501.
40 L. Svennerholm, *J. Lipid Res.*, 1968, **9**, 570–579.
41 B. Bonev, A. Watts, M. Bokvist and G. Gröbner, *Phys. Chem. Chem. Phys.*, 2001, **3**, 2904–2910.
42 J. J. Kremer and R. M. Murphy, *J. Biochem. Biophys. Methods*, 2003, **57**, 159–169.
43 S. Dante, T. Hauss and N. A. Dencher, *Biophys. J.*, 2002, **83**, 2610–2616.
44 O. Simakova and N. J. Arispe, *Biophys. J.*, 2012, **102**, 657a.
45 C. H. Davis and M. L. Berkowitz, *Biophys. J.*, 2009, **96**, 785–797.
46 B. R. Sahoo, T. Genjo, S. J. Cox, A. K. Stoddard, G. M. Anantharamaiah, C. Fierke and A. Ramamoorthy, *J. Mol. Biol.*, 2018, **430**, 4230–4244.
47 J. Pilch, C. M. Franzin, L. M. Knowles, F. J. Ferrer, F. M. Marassi and E. Ruoslahti, *J. Mol. Biol.*, 2006, **356**, 876–885.
48 G. Lee, H. B. Pollard and N. Arispe, *Peptides*, 2002, **23**, 1249–1263.
49 V. Martín, N. Fabelo, G. Santpere, B. Puig, R. Marín, I. Ferrer and M. Díaz, *J. Alzheimer's Dis.*, 2010, **19**, 489–502.
50 S. Banerjee, M. Hashemi, K. Zagorski and Y. L. Lyubchenko, *ACS Chem. Neurosci.*, 2021, **12**, 506–516.
51 L. Qiu, A. Lewis, J. Como, M. W. Vaughn, J. Huang, P. Somerharju, J. Virtanen and K. H. Cheng, *Biophys. J.*, 2009, **96**, 4299–4307.
52 D. Frankel, M. Davies, B. Bhushan, Y. Kulaberoglu, P. Urriola-Munoz, J. Bertrand-Michel, M. R. Pergande, A. A. Smith, S. Preet, T. J. Park, M. Vendruscolo, K. S. Rankin, S. M. Cologna, J. R. Kumita, N. Cenac and E. St John Smith, *Aging*, 2020, **12**, 22266–22290.
53 W. Wood, F. Schroeder, U. Igbavboa, N. Avdulov and S. Chochina, *Neurobiol. Aging*, 2002, **23**, 685–694.
54 C. E. Heo, C. R. Park and H. I. Kim, *Chem. Phys. Lipids*, 2021, **236**, 105073.
55 V. Dubois, D. Serrano and S. Seeger, *ACS Chem. Neurosci.*, 2019, **10**, 4776–4786.
56 J. Lee, Y. H. Kim, F. T. Arce, A. L. Gillman, H. Jang, B. L. Kagan, R. Nussinov, J. Yang and R. Lal, *ACS Chem. Neurosci.*, 2017, **8**, 1348–1357.
57 S. Meker, H. Chin, T. N. Sut and N.-J. Cho, *Langmuir*, 2018, **34**, 9548–9560.
58 D. Mrdenovic, M. Majewska, I. S. Pieta, P. Bernatowicz, R. Nowakowski, W. Kutner, J. Lipkowski and P. Pieta, *Langmuir*, 2019, **35**, 11940–11949.

59 Y. Tian, R. Liang, A. Kumar, P. Szwedziak and J. H. Viles, *Chem. Sci.*, 2021, **12**, 6896–6907.
60 Y.-H. M. Chan and S. G. Boxer, *Curr. Opin. Chem. Biol.*, 2007, **11**, 581–587.
61 J. Robinson, G. B. Berselli, M. G. Ryadnov and T. E. Keyes, *Langmuir*, 2020, **36**, 5454–5465.
62 G. B. Berselli, A. V. Gimenez, A. O'Connor and T. E. Keyes, *ACS Appl. Mater. Interfaces*, 2021, **13**, 29158–29169.
63 G. B. Berselli, N. K. Sarangi, S. Ramadurai, P. V. Murphy and T. E. Keyes, *ACS Appl. Bio Mater.*, 2019, **2**, 3404–3417.
64 N. K. Sarangi, A. Prabhakaran and T. E. Keyes, *Electroanalysis*, 2020, **32**, 2936–2945.
65 H. Basit, V. Gaul, S. Maher, R. J. Forster and T. E. Keyes, *Analyst*, 2015, **140**, 3012–3018.
66 S. Maher, H. Basit, R. J. Forster and T. E. Keyes, *Bioelectrochemistry*, 2016, **112**, 16–23.
67 N. K. Sarangi, A. Stalcup and T. E. Keyes, *ChemElectroChem*, 2020, **7**, 4535–4542.
68 N. K. Sarangi, A. Prabhakaran and T. E. Keyes, *Langmuir*, 2022, **38**, 6411–6424.
69 K. Broersen, W. Jonckheere, J. Rozenski, A. Vandersteen, K. Pauwels, A. Pastore, F. Rousseau and J. Schymkowitz, *Protein Eng., Des. Sel.*, 2011, **24**, 743–750.
70 D. Mrdenovic, P. Zarzycki, M. Majewska, I. S. Pieta, R. Nowakowski, W. Kutner, J. Lipkowski and P. Pieta, *ACS Chem. Neurosci.*, 2021, **12**, 531–541.
71 Y. Sokolov, J. A. Kozak, R. Kayed, A. Chanturiya, C. Glabe and J. E. Hall, *J. Gen. Physiol.*, 2006, **128**, 637–647.
72 W. B. Stine, K. N. Dahlgren, G. A. Krafft and M. J. LaDu, *J. Biol. Chem.*, 2003, **278**, 11612–11622.
73 S. Banerjee, M. Hashemi, K. Zagorski and Y. L. Lyubchenko, *Int. J. Mol. Sci.*, 2020, **21**, 1129.
74 A. Tiiman, J. Krishtal, P. Palumaa and V. Tõugu, *AIP Adv.*, 2015, **5**, 092401.
75 S. Ramadurai, A. Kohut, N. K. Sarangi, O. Zholobko, V. A. Baulin, A. Voronov and T. E. Keyes, *J. Colloid Interface Sci.*, 2019, **542**, 483–494.
76 S. Ramadurai, N. K. Sarangi, S. Maher, N. MacConnell, A. M. Bond, D. McDaid, D. Flynn and T. E. Keyes, *Langmuir*, 2019, **35**, 8095–8109.
77 S. Ramadurai, M. Werner, N. K. H. Slater, A. Martin, V. A. Baulin and T. E. Keyes, *Soft Matter*, 2017, **13**, 3690–3700.
78 A. Bouter, C. Gounou, R. Bérat, S. Tan, B. Gallois, T. Granier, B. L. D'Estaintot, E. Pöschl, B. Brachvogel and A. R. Brisson, *Nat. Commun.*, 2011, **2**, 270.
79 M. A. Johnson, S. Seifert, H. I. Petrache and A. C. Kimble-Hill, *Langmuir*, 2014, **30**, 9880–9885.
80 M. E. Haque, T. J. McIntosh and B. R. Lentz, *Biochemistry*, 2001, **40**, 4340–4348.
81 V. Gerke and S. E. Moss, *Physiol. Rev.*, 2002, **82**, 331–371.
82 F. Oling, J. S. O. Santos, N. Govorukhina, C. Mazères-Dubut, W. Bergsma-Schutter, G. Oostergetel, W. Keegstra, O. Lambert, A. Lewit-Bentley and A. Brisson, *J. Mol. Biol.*, 2000, **304**, 561–573.
83 C. Pigault, A. Follenius-Wund, M. Schmutz, J.-M. Freyssinet and A. Brisson, *J. Mol. Biol.*, 1994, **236**, 199–208.
84 F. Oling, W. Bergsma-Schutter and A. Brisson, *J. Struct. Biol.*, 2001, **133**, 55–63.
85 H.-Y. Kim, B. X. Huang and A. A. Spector, *Prog. Lipid Res.*, 2014, **56**, 1–18.
86 L.-F. Lue, Y.-M. Kuo, A. E. Roher, L. Brachova, Y. Shen, L. Sue, T. Beach, J. H. Kurth, R. E. Rydel and J. Rogers, *Am. J. Pathol.*, 1999, **155**, 853–862.
87 K. Rajasekhar, M. Chakrabarti and T. Govindaraju, *Chem. Commun.*, 2015, **51**, 13434–13450.
88 J. R. Cirrito, P. C. May, M. A. O'Dell, J. W. Taylor, M. Parsadanian, J. W. Cramer, J. E. Audia, J. S. Nissen, K. R. Bales, S. M. Paul, R. B. DeMattos and D. M. Holtzman, *J. Neurosci.*, 2003, **23**, 8844–8853.
89 D. Puzzo, L. Privitera, M. Fa, A. Staniszewski, G. Hashimoto, F. Aziz, M. Sakurai, E. M. Ribe, C. M. Troy, M. Mercken, S. S. Jung, A. Palmeri and O. Arancio, *Ann. Neurol.*, 2011, **69**, 819–830.
90 G. M. J. A. Klug, D. Losic, S. Subasinghe, M.-I. Aguilar, L. L. Martin and D. H. Small, *Eur. J. Biochem.*, 2003, **270**, 4282–4293.
91 K. Garai, R. Sureka and S. Maiti, *Biophys. J.*, 2007, **92**, L55–L57.
92 M. Sublimi Saponetti, M. Grimaldi, M. Scrima, C. Albonetti, S. L. Nori, A. Cucolo, F. Bobba and A. M. D'Ursi, *PLoS One*, 2014, **9**, e115780.
93 B. Soreghan, J. Kosmoski and C. Glabe, *J. Biol. Chem.*, 1994, **269**, 28551–28554.
94 M. Zhu, P. O. Souillac, C. Ionescu-Zanetti, S. A. Carter and A. L. Fink, *J. Biol. Chem.*, 2002, **277**, 50914–50922.
95 W. K. Chang, W. C. Wimley, P. C. Searson, K. Hristova and M. Merzlyakov, *Biochim. Biophys. Acta, Biomembr.*, 2008, **1778**, 2430–2436.
96 P. Zimmermann, K. Schlenstedt, S. Schwarz, D. Vehlow, M. Blanke, A. Fery and J. Nagel, *ACS Appl. Polym. Mater.*, 2022, **4**, 5189–5198.
97 Z. Chen, Y. Wang, Y. Shang, A. Umar, P. Xie, Q. Qi and G. Zhou, *Sci. Rep.*, 2017, **7**, 2713.
98 N. Tarutani, Y. Tokudome, K. Nakanishi and M. Takahashi, *RSC Adv.*, 2014, **4**, 16075–16080.
99 K. Sasahara, K. Morigaki and K. Shinya, *Phys. Chem. Chem. Phys.*, 2013, **15**, 8929.
100 N. P. Reynolds, A. Soragni, M. Rabe, D. Verdes, E. Liverani, S. Handschin, R. Riek and S. Seeger, *J. Am. Chem. Soc.*, 2011, **133**, 19366–19375.
101 S. Sugimoto, K. Arita-Morioka, Y. Mizunoe, K. Yamanaka and T. Ogura, *Nucleic Acids Res.*, 2015, **43**, e92–e92.
102 C. Xue, T. Y. Lin, D. Chang and Z. Guo, *R. Soc. Open Sci.*, 2017, **4**, 160696.